PHOTOLUMINESCENCE SPECTRA OF EMERALDS FROM COLOMBIA, AFGHANISTAN, AND ZAMBIA

D. Brian Thompson, Christian J. Bayens, Matthew B. Morgan, Taylor J. Myrick, and Nealey E. Sims

Laser-excited photoluminescence spectra were collected from 48 emeralds originating from Colombia, Afghanistan, and Zambia. Photoluminescence in emerald arises from trace chromium impurities, and its spectrum displays two narrow *R* lines overlaid upon a broadband signal. In the collected spectra, peak positions of these *R* lines varied across a small range of wavelengths; the origin-dependent nature of these variations may be helpful in identifying the geographic source of unknown samples. Comparisons between *R*-line peak wavelengths and corresponding trace element concentrations of samples revealed strong correlations between peak shifts of the R_1 line and increases in magnesium and sodium concentrations, and between peak shifts of the R_2 line and increases in lithium and sodium concentrations. These correlations suggest that substitution defects of magnesium for aluminum with sodium impurities may be responsible for the R_1 line peak shifts, and similar defects of lithium for beryllium with sodium impurities may be responsible for the R_2 line peak shifts. Finally, a comparison between photoluminescence count rates and chromium and iron concentrations showed that count rates decrease exponentially with increasing iron concentration.

Emerald (figure 1) is a gem variety of beryl ($Be_3Al_2Si_6O_{18}$), whose green color arises from trace impurities of chromium and/or vanadium. While pure beryl is colorless, the trace amounts of Cr and V ions absorb light in the red and blue-violet region of the visible spectrum to produce emerald's green color (Schwarz and Schmetzer, 2002). Emeralds may also contain trace amounts of iron; this chromophore ion, also responsible for colors seen in the heliodor and aquamarine varieties of beryl (Nassau, 1978), may add a yellow or blue tint.

Some of the visible light energy absorbed by emerald's Cr ions can reappear as red photoluminescence (Nassau, 1978). This photoluminescence (PL) is usually not bright enough to be seen under normal lighting conditions. Illuminating an emerald with green monochromatic laser light produces a PL reaction that can be observed when the excitation light is blocked by a color filter (figure 2). Laser-excited PL spectra of emerald (figure 3) contain a broadband structure, peaking at about 715 nm, that results from a Stokes-shifted reversal of the electron transition

Figure 1. Emerald crystals from Colombia (top right), Afghanistan (bottom right), and Zambia (left). Each emerald's hexagonal prismatic crystal habit has been enhanced by polishing flat the two hexagonal end faces (perpendicular to the crystal's c-axis) and two or more prism sides (parallel to the c-axis). Photo by D.B. Thompson.

See end of article for About the Authors and Acknowledgments.
GEMS & GEMOLOGY, Vol. 53, No. 3, pp. 296–311,
http://dx.doi.org/10.5741/GEMS.53.3.296

Figure 2. With a green laser beam illuminating it from the left, and a color filter positioned in front to remove green light, an emerald crystal (center) is seen to emit red photoluminescence. Photo by D.B. Thompson.

that produces emerald's red absorption band (Lai, 1987). Superimposed upon this structure are two narrow lines that arise from electronic decay of a doublet metastable state, known as *R* lines (Wood, 1965). These *R* lines also appear in emerald absorption spectra, where the longer-wavelength line (denoted R_1) peaks at around 683 nm and the shorter-wavelength line (R_2) peaks at around 680 nm (Wood, 1965).

In Brief

- The *R* lines appearing in PL spectra of emeralds specimens from Colombia, Afghanistan, and Zambia show peak shifts that depend upon geographic source.
- Comparisons between emerald specimens' *R*-line peak wavelengths and their atomic impurity concentrations suggest which trace elements are responsible for the observed peak shifts.
- An emerald's PL emission intensity increases with atomic chromium concentration and decreases exponentially with atomic iron concentration.
- *R*-line peak measurements show promise as an aid in determining the geographic origin of emeralds.

Moroz et al. (2000) collected PL spectra from natural emeralds from nine deposits, as well as from a synthetic emerald. In their PL spectra, the peak positions of the *R* lines of emeralds from schist-host deposits showed moderate shifts in wavelength compared to those lines from emeralds originating from other types of deposits. The authors suggested that these wavelength shifts might be caused by Mg or Fe ions substituting at Al sites, based on the principle that these impurities occur at higher concentrations in schist-origin emeralds.

Recently, Thompson et al. (2014) collected PL spectra of natural emeralds from 11 different localities and synthetic emeralds from four different sources. The results confirmed observations made by Moroz et al. (2000): R_1 lines of synthetic emeralds peak at the shortest wavelengths, while in natural non-schist emeralds this line peaks at the same or longer wavelengths. In schist-origin emeralds the line peaks at an even longer wavelength, with peak positions spread across a range on the order of 1.0 nm. By comparison, the spread of R_2 lines of most emeralds fell within a 0.2 nm range, though some schist-origin emeralds had R_2 lines shifted up to 0.3 nm outside this range toward shorter wavelengths.

Thompson et al. (2014) compared their natural emeralds' R_1-line wavelengths to chemical composition measurements of a different set of emeralds with the same origin, and observed correlation between R_1-line wavelengths and SiO_2 weight concentrations. The authors suggested that R_1 line shifts might arise from impurity substitutions at Si crystal sites in

Figure 3. Photoluminescence (PL) spectra of emerald samples from the selected countries of origin were collected with the polarization axis of the excitation laser light aligned perpendicular to the crystal's c-axis. The black trace is from the Colombian sample shown in figure 1, the red trace from the Afghan sample, and the blue trace from the Zambian sample.

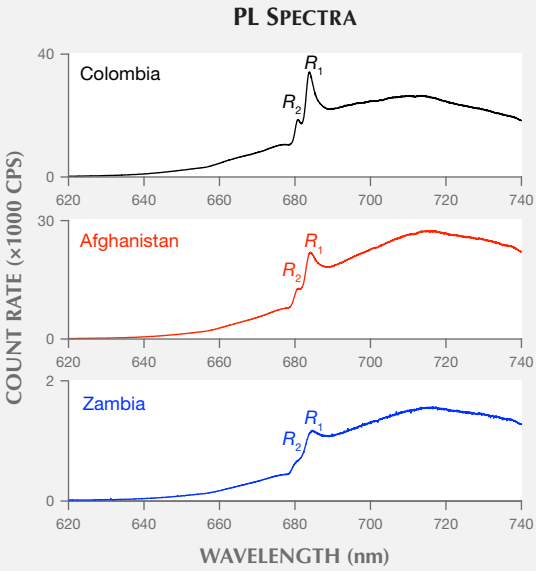

emerald. This speculation was incorrect, as an earlier X-ray diffraction study of beryl (Aurisicchio et al., 1988) found no evidence for substitution defects occurring at Si crystal sites in any type of natural or synthetic beryl. Schmetzer and Bernhardt (1994), and more recently Schmetzer (2015), showed that the minor reductions in Si weight concentrations in emerald could arise from an accrual of substitutions at Al crystal sites.

While Aurisicchio et al. (1988) found no ion substitutions at Si tetrahedral sites in beryl, they examined the other beryl crystal cation sites and did find that two types of substitutions can occur at Al octahedral sites. One is isovalent substitution, where the Al ion is replaced by another trivalent cation. Using Schmetzer's (2015) notation, this substitution can be written as

$$Al^{3+} \leftrightarrow Me^{3+} (Me^{3+} = V, Cr, Mn, Fe, etc.)$$

The other type is an aliovalent substitution, where the Al ion is replaced by a divalent cation. This substitution is accompanied by an alkali ion to provide charge compensation, where the alkali ion occupies an interstitial site within the beryl's open channels parallel to the c-axis (Goldman et al., 1978). This substitution can be written as

$$Al^{3+} \leftrightarrow Me^{2+} + Me^{+} (Me^{2+} = Mg, Mn, Fe, etc., \text{ and } Me^{+} = Li, Na, K, Cs, etc.)$$

Only a single substitution is possible at the tetrahedral site, the aliovalent substitution:

$$Be^{2+} \leftrightarrow Li^{+} + Me^{+} (Me^{+} = Li, Na, K, Cs, etc.)$$

Here the Be ion is replaced by a Li ion, accompanied by another alkali ion occupying an open channel site to provide charge compensation. While Aurisicchio et al. found that this substitution is common in some varieties of beryl, they did not observe significant occurrence of this substitution in emerald.

Saeseaw et al. (2014) performed microscopic, spectroscopic, and trace element analysis of emeralds with three-phase inclusions. Here we examine their samples from Colombia, Afghanistan, and Zambia. These samples are of interest because of the different geologies in which they formed. Colombian emeralds formed through hydrothermal processes in sedimentary shale, whereas Zambian emeralds are found in metamorphic phlogopite schists. The Afghan emeralds are hosted in metamorphic-metasomatic phlogopite schists subjected to strong hydrothermal processes (Groat et al., 2008; Giuliani et al., 2012). In short, Afghan emerald formed in a process similar to that which formed Colombian emeralds, but within host material similar to Zambian emeralds. As a result, the Colombian and Zambian emeralds exhibit distinctly different concentrations of several trace impurities, while impurity concentrations in Afghan emeralds bridge these two extremes (Saeseaw et al., 2014).

This study expands upon the work of Thompson et al. (2014) and presents *R*-line peak wavelength results derived from PL spectra of 48 Colombian, Afghan, and Zambian emerald samples prepared by GIA's laboratory in Bangkok; most of these samples were also used in Saeseaw et al. (2014). The present study demonstrates that the accumulation of *R*-line peak wavelength data from samples of known origin can provide evidence for or against various geographic origins. The peak wavelength data are compared with the samples' trace impurity concentrations to iden-

TABLE 1. Chemical composition of emerald samples (ppma), as measured by LA-ICP-MS.

	Colombia	Afghanistan	Zambia
^{7}Li	90–345 (173)	225–596 (301)	1280–2323 (1704)
^{9}Be	91,359–118,638 (108,826)	96,325–120,710 (107,886)	90,388–122,046 (106,214)
^{23}Na	1037–6730 (3382)	4621–10,646 (8053)	11,482–14,262 (13,365)
^{24}Mg	1021–6076 (3034)	3683–10,070 (7299)	9804–13,946 (11,762)
^{27}Al	57,790–75,526 (66,762)	53,057–70,257 (62,230)	48,171–62,381 (55,249)
Si normalized value	(206,897)	(206,897)	(206,897)
^{39}K	0–13 (3)	63–612 (316)	172–300 (243)
^{45}Sc	2–83 (30)	27–880 (225)	6–41 (19)
^{51}V	116–1731 (618)	93–1264 (488)	30–72 (42)
^{53}Cr	83–677 (295)	79–1432 (651)	357–1427 (924)
^{57}Fe	69–723 (219)	380–3153 (1439)	2252–3834 (3069)
^{133}Cs	1–2 (1)	3–12 (7)	0–207 (149)

Analyses were performed at GIA's Bangkok lab. Data are reported in minimum and maximum values, with average concentration in parentheses, and assume ideal oxygen concentration of 535,782 ppma. Alkali and transition metals with less than 25 ppma for all samples are not included in the table.

tify which trace impurities might be responsible for shifting *R*-line peak wavelengths. The study concludes with a comparison between Cr and Fe concentrations and broadband PL emission intensity to quantify the role each element plays in emerald photoluminescence.

MATERIALS AND METHODS

We collected PL spectra from 48 emerald samples on loan from GIA's Bangkok laboratory. Twenty of the samples were from the Coscuez and Muzo mines in the Boyacá region of Colombia, separated by about 10 km; 16 samples from two mines, Kameer Safeed and Koskanda, in the Khendj area of Afghanistan's Panjsher region, separated by less than 1 km; and 12 samples from the Kagem mine in the Kafubu area of Zambia. Forty-five of these samples were used in the work by Saeseaw et al. (2014), while one Afghan sample and two Zambian samples were used for the first time in this report. As outlined by Saeseaw et al. (2014), GIA altered its emeralds from their original rough form by polishing one or two flat surfaces perpendicular to each crystal's c-axis; some also have flat surfaces polished parallel to the c-axis. A specialized tool designed to locate the c-axis of a specimen (Thomas, 2009) was used to align the samples for polishing these flat surfaces.

As Saeseaw et al. (2014) describe, GIA's Bangkok laboratory determined the chemical composition of each emerald sample using laser ablation–inductively coupled plasma–mass spectrometry (LA-ICP-MS). For quantitative analysis, the spectrometer was

Figure 4. The experimental setup showing laser output (bottom left) and the optical fiber with collimating lens (top left) facing the beam path. The other end of the optical fiber connects to a CCD spectrometer (not shown). An emerald sample sits upon the suction cup of a vacuum pen. The pen itself is held in a rotation mount (upper right), which is attached to an XYZ translation stage (partially visible). With the crystal oriented as shown, the laser beam will cross its polished end face at normal incidence. The inset shows the laser's circular beam spot (in blue) positioned at the edge of the crystal face closest to the collection lens. The beam itself is parallel to the crystal's c-axis, and the beam's polarization axis E is perpendicular to the c-axis. This is the typical orientation used to collect E⊥c photoluminescence spectra. Photo by D.B. Thompson.

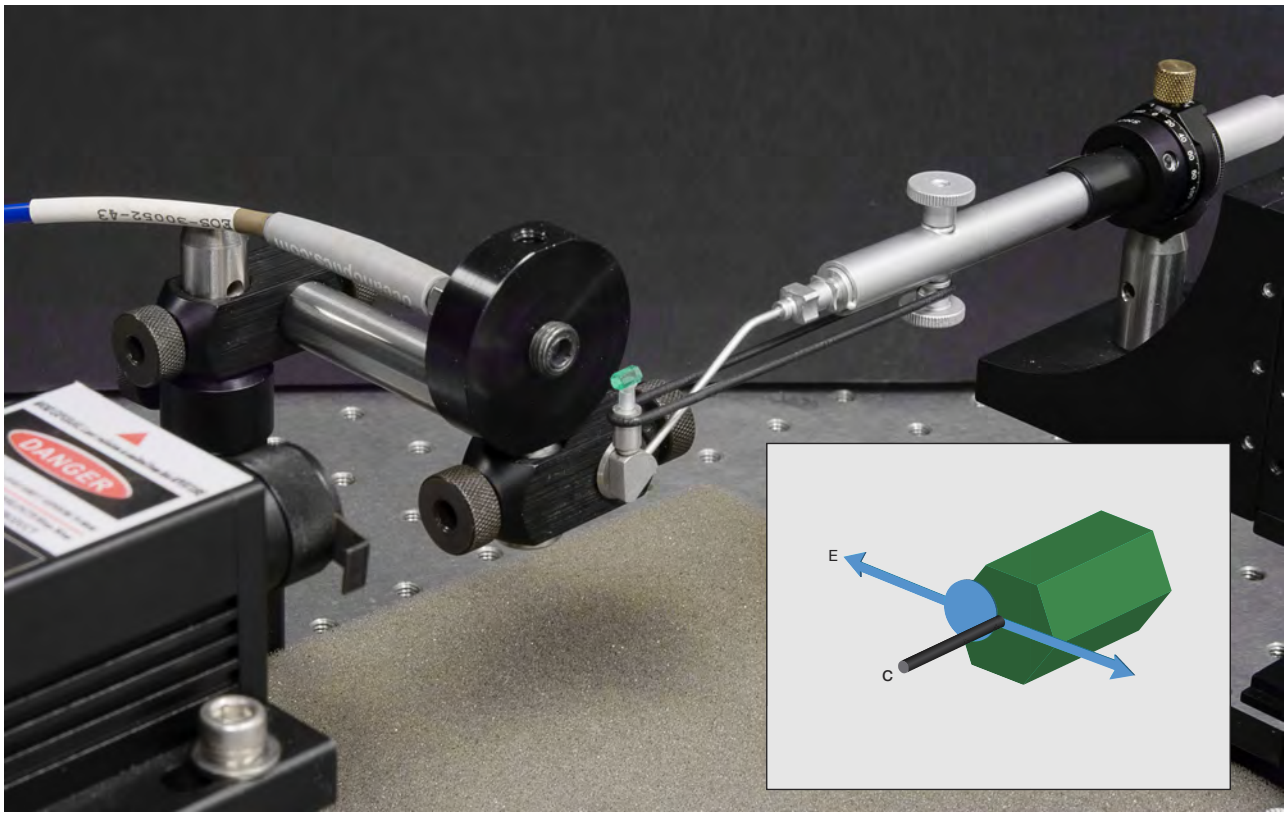

calibrated using NIST 610 and 612 glasses with known concentrations of elements. Along with providing the emerald samples, GIA also supplied their chemical composition measurements (table 1).

The experimental setup for collecting PL spectra (figure 4) has been described previously (Thompson et al., 2014). A continuous-wave diode pumped solid state (DPSS) laser (Laserglow LRS-532-TM-100-10) emits a 100 mW, 532 nm beam with horizontal polarization. Then a 0.5 mm diameter optical fiber with a 25° field-of-view collimating lens, mounted perpendicular to the laser beam, collects PL emission at room temperature from an emerald sample placed within the overlap region between the laser beam and collection lens field of view. The PL emission collected by the fiber enters a charge-coupled device (CCD) spectrometer (Ocean Optics USB4000) with a custom grating that disperses light over the 580–740 nm wavelength range; this spectrometer has full width at half maximum (FWHM) resolution of 0.20 nm, and the average width of each spectrometer channel is 0.045 nm. Discrete line emissions from argon and neon spectral lamps were used to calibrate the spectrometer's wavelength scale.

For this study, one change was made to the previous setup: A vacuum pen (Dazor SPK-100-VPEN) was used to position the emeralds. The pen's pulley system allows complete rotation of the sample about an axis through the stone. The pen itself is held in another rotation mount to allow rotation of the sample about a second, orthogonal axis. In turn, the rotation mount is attached to an XYZ translation stage with at least 13 mm of travel in three orthogonal directions. This assembly provides fine control for positioning a sample so that the laser beam can intersect any point along its surface (not obscured by the pen's vacuum suction cup) at any incident angle.

Emerald is optically uniaxial, and PL emission spectra collected when the excitation laser beam's polarization axis is perpendicular to the crystal's c-axis ($E \perp c$) differ from those collected with the beam's polarization axis parallel to the c-axis ($E \parallel c$). Both R_1 and R_2 peak positions change, as does the R_1/R_2 peak height ratio, as described in box A. Emeralds from different localities show the largest quantitative variations for these peak parameters when the spectra are collected with $E \perp c$ beam-crystal axes orientation. Therefore, the current study only considers spectra collected with $E \perp c$ beam-crystal axes orientation.[1]

To collect a PL spectrum with $E \perp c$ orientation, the sample itself is positioned so that the excitation laser beam enters a flat surface polished perpendicular to the crystal's c-axis at normal incidence. With this orientation, the excitation laser beam's polarization axis is also perpendicular to the crystal's c-axis. The sample is always positioned so that the beam overlaps the emerald edge closest to the optical fiber's collection lens (again, see figure 4). This sampling position was chosen to minimize PL emission traveling through unilluminated emerald before entering the fiber.

To construct each sample's PL spectrum, 100 accumulated scans were averaged; each scan's typical integration time was one second. In a similar manner, with the laser shuttered, a "dark" spectrum was produced. The final PL spectrum was created by subtracting the so-called dark spectrum from the sample spectrum. Doing so reduced counting noise arising from thermal motion of electrons in the spectrometer's CCD.

These emerald PL spectra (e.g., figure 3) exhibit local minima on either side of the *R* lines. To isolate the *R*-line contribution in each PL spectrum, a baseline is subtracted from the data. The line's endpoints at 678.5 and 688.5 nm were selected to coincide with these local minima. The resulting spectra (e.g., figure 5) are referred to as *R*-line spectra.

The *R*-line spectra in figure 5 each show two lines with width and peak separation at least an order of magnitude larger than the spectrometer's resolution. Besides the two peaks, no other fine structure appears in the spectra. After creating an *R*-line spectrum, peak-finding software (O'Haver, 2014) was used to extract R_1 and R_2 peak wavelengths and corresponding count rates, which were used to determine an R_1/R_2 peak height ratio. The R_1 and R_2 peak wavelengths reported here are means of values extracted from four separate spectral measurements. The resulting uncertainty in peak position is ±0.02 nm, as given by the four measurements' standard deviation of the mean.

The first step in analyzing the *R*-line datasets was to examine how *R*-line peak wavelength distributions vary with sample origins. This is done by performing independent sample *t* tests on *R*-line peak

[1] GIA's laboratory in Bangkok prepared the samples used here with c-axes aligned perpendicular to polished crystal faces, so that arranging a crystal for collection of E⊥c PL spectra (e.g., figure 4) was straightforward. An E⊥c PL spectrum can also be collected from a cut emerald even when its c-axis is not aligned perfectly perpendicular to its table facet; the strong variation of R_1/R_2 peak height ratio described in box A can be employed systematically to locate an E⊥c alignment through the table of any cut emerald sample.

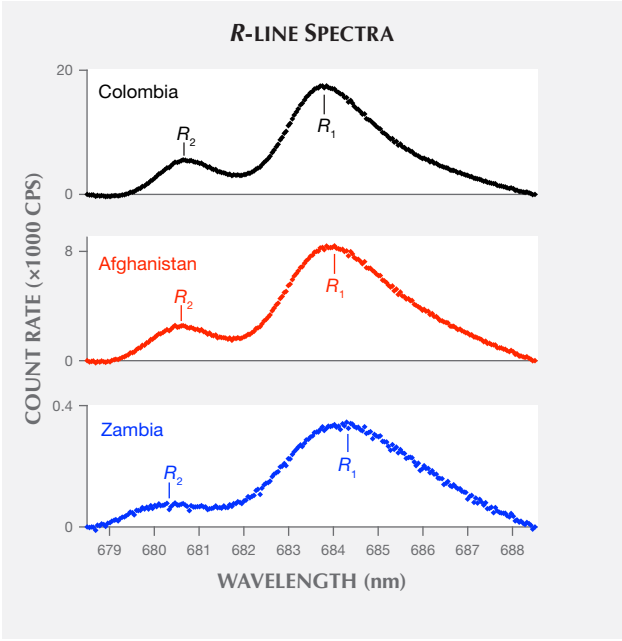

Figure 5. R-*line spectra of emerald samples resulting from the baseline subtraction of PL spectra in figure 3.* R_1 *is defined as the line at the center of the peak at the longer wavelength, and* R_2 *is defined as the line at the center of the peak of the shorter wavelength.*

wavelength values from samples with two different geographic origins (Crow et al., 1960). The Discussion section contains examples of how a random sample's measured *R*-line wavelength can be compared with measured distributions to either support or reject possible origins.

We then determined whether a linear relation exists between *R*-line peak wavelengths and concentrations of a particular trace element by calculating the coefficient of determination r^2 between the two datasets. In linear regression analysis of two variables, the coefficient of determination represents the fraction of variance of one dataset that is predictable from a "best-fit" linear relation with the other dataset (Crow et al., 1960). The coefficient of determination can range between 0 and 1, and two datasets are identified as strongly correlated when the coefficient of determination between them has a value $r^2 \geq 0.64$.

An issue arises from comparing *R*-line peak wavelengths extracted from the PL spectra to the trace element concentrations measured by LA-ICP-MS. In particular, the laser-illuminated volume in a sample that produces PL may not coincide with the surface spots where laser ablation was applied for mass spectrometry. This is a concern because trace element concentrations in natural emerald crystals can, and generally do, vary throughout the samples (Schmetzer, 1994; Schmetzer and Bernhardt, 1994). As a result, the LA-ICP-MS spot measurements of trace element concentrations may not perfectly match average concentrations within the bulk PL emission volume. This can reduce coefficients of determination between *R*-line parameters and trace element concentrations, leading to outliers in the resulting scatterplots.

In this report, scatterplots are presented for the *R*-line peak wavelength vs. trace element concentration datasets that demonstrate the highest coefficients of determination (i.e., strongest correlation). Next, linear regression is used to find each scatterplot's "best-fit" trend line, where the slope of this line corresponds to the pairwise variation of the dataset, and where its intercept identifies the *R*-line's peak wavelength for zero concentration of the trace element.

RESULTS

Examining *R*-line spectra extracted from the emeralds' PL spectra (figure 5), we see that the Colombian sample's R_1 line peaks at the shortest wavelength, the Afghan sample's line at a longer wavelength, and the Zambian sample's line at the longest wavelength. A plot of the mean R_1 peak wavelength of samples from each origin (figure 6) shows that this origin-based peak shift holds true on average. An overlap between Afghan and Colombian samples, seen in figure 6, results from a single anomalous R_1 peak wavelength value in each origin's dataset.

To compare R_1 peak wavelength distributions between Colombian and Afghan samples, we performed an independent sample *t* test. The *t* test uses the following values from each geographic sample's wavelength distribution: number of samples (N), mean wavelength value (M), and the standard deviation (SD) of these values. The *t* test produces a *t* value, t(df), where df represents the degrees of freedom. One then uses the *t* value to determine fractional probability (*p*) that the two populations share the same mean value, and to determine the 95% confidence interval (95% CI) for the difference between their mean values. The results show extremely significant differences in the distributions for the Colombian (N = 20, M = 683.777 nm, SD = 0.060 nm) and Afghan samples (N = 16, M = 684.013 nm, SD = 0.084 nm); t(34) = 9.88, $p < 0.0001$, and 95% CI [0.188 nm, 0.285 nm]. The low *p* value between this pair of sample datasets suggests that the measured difference between their mean peak wavelengths probably does not arise from an accident of sampling.

BOX A: VARIATIONS OF *R*-LINE PARAMETERS WITH THE ORIENTATION ANGLE BETWEEN EMERALD C-AXIS AND LASER BEAM POLARIZATION

Moroz et al. (2000) collected PL spectra from emerald samples with the excitation laser beam's polarization axis parallel to the crystal's c-axis (E ∥ c) and with the beam's polarization axis perpendicular to the c-axis (E ⊥ c). Comparing an emerald's E ∥ c orientation PL spectrum to its E ⊥ c orientation spectrum, the R_1 and R_2 peak positions and relative peak intensities both differ.

Thompson et al. (2014) rotated a rough emerald sample with hexagonal prismatic crystal habit in a laser beam from an E ∥ c orientation to E ⊥ c orientation while collecting PL spectra at 10° intervals. From these spectra, they extracted angular distributions of R_1 and R_2 peak positions and R_1/R_2 peak height ratios. These angular distributions showed that the R_1/R_2 peak height ratios varied smoothly from a minimum value around 1 when E ∥ c to a maximum value around 3 when E ⊥ c. They also showed that the R_1 and R_2 peak positions were relatively constant at angles around the E ⊥ c orientation, but varied rapidly at angles midway between E ⊥ c and E ∥ c orientations.

As noted in the text, we extracted R_1 and R_2 peak positions from E ⊥ c PL spectra of emeralds to compare with their impurity concentrations. To verify the consistency of these peak position values even under slightly imperfect orientation of the sample's c-axis relative to the excitation beam's polarization direction, here we reproduce the procedure outlined by Thompson et al. (2014) for collecting angular distributions of these parameters. The procedure was carried out using a hexagonal prismatic crystal sample from each of the three geographic origins (again, see figure 1). The c-axis of these samples lay parallel to the prism's central axis and perpendicular to the end faces.

Initially, each sample's c-axis was aligned parallel to the laser light's horizontal polarization axis and perpendi-

Figure A-1. Examples of emerald orientations used to collect PL spectra at different angles between the crystal's c-axis and the laser beam's polarization axis. The top row shows the crystal's c-axis oriented parallel with the laser beam's horizontal polarization axis, creating the E ∥ c orientation. With the fiber-optic collection lens located to the left of the sample, the laser illuminates the bottom left edge of the emerald. The middle row shows the crystal's c-axis at a 50° angle from the beam's polarization axis. The same edge region of the crystal is illuminated by laser light. The bottom row shows the crystal's c-axis perpendicular to the beam's polarization axis, creating an E ⊥ c orientation. Once again, the same edge region of the crystal is illuminated. Photos by D.B. Thompson.

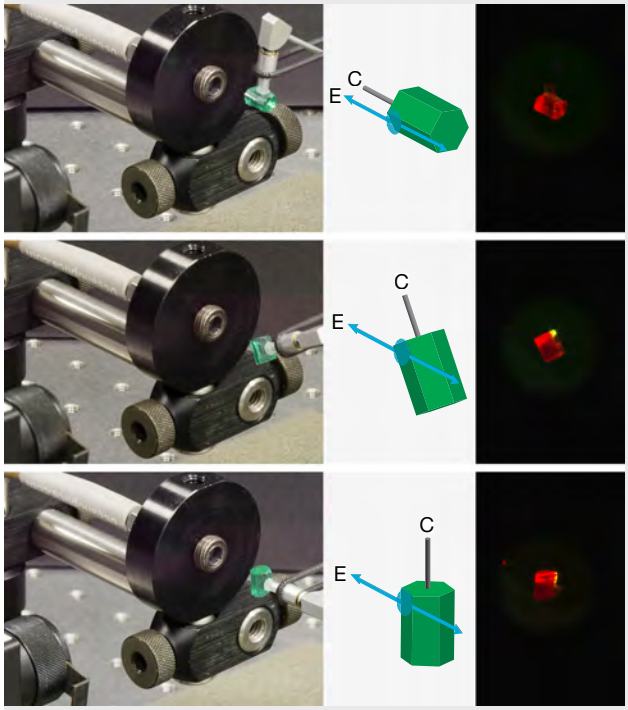

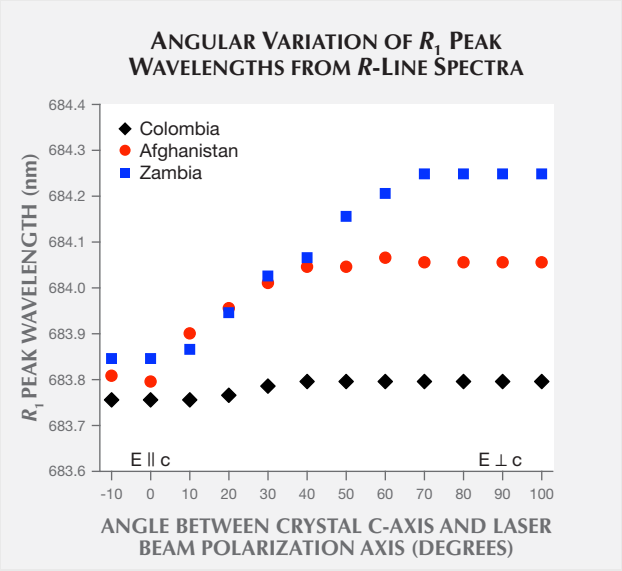

Figure A-2. The angular variation of R_1 *peak wavelengths extracted from* R*-line spectra of emerald crystals from the three geographic origins.*

cular to the laser beam propagation direction itself to create the E ∥ c orientation. Then the sample's c-axis could be rotated to create any angle between it and the laser's polarization axis, including the E ⊥ c orientation (see figure A-1). For each sample, the procedure involves collecting 12 PL spectra at 10° intervals, ranging from 10° below E ∥ c to 10° above the E ⊥ c orientation. As described in the text, we isolated the *R*-line contribution from each spectrum to create an *R*-line spectrum, from which we extracted R_1 and R_2 peak positions and count rates.

Plotting each sample's R_1 peak positions on an angular scale (figure A-2), it is readily apparent that the peak wavelengths of samples from the three different geographic regions exhibit a much wider spread in the E ⊥ c orientation than the E ∥ c orientation. For all three samples, the value of the R_1 peak wavelength is constant for angles between E and c-axes from E ⊥ c to 70°. Below that angular range, the peak wavelength varies continuously through to the E ∥ c orientation.

A plot of each sample's R_2 peak positions on an angular scale (figure A-3) shows that the Colombian and Afghan samples have nearly the same set of peak wavelength values across the angular range, while the Zambian sample's peak positions occur at consistently lower wavelengths. As with the R_1 line, the value of the R_2 peak wavelength for all three samples remains relatively constant up to 20° away from the E ⊥ c orientation.

Figure A-3. The angular variation of R_2 *peak wavelengths extracted from* R*-line spectra of emerald crystals from the three geographic origins.*

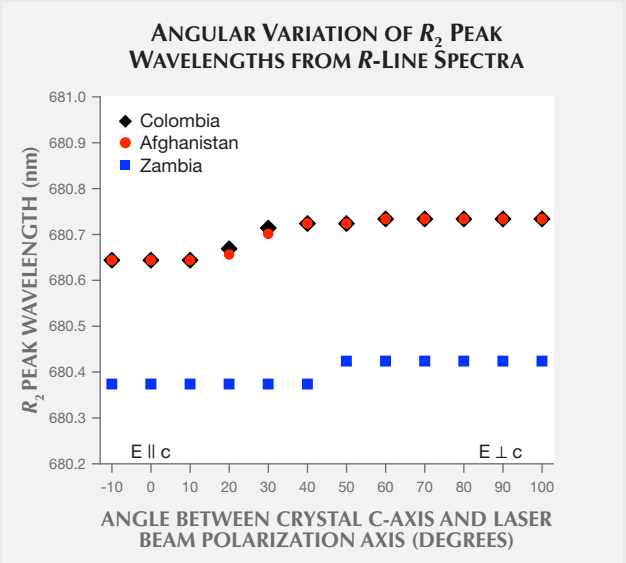

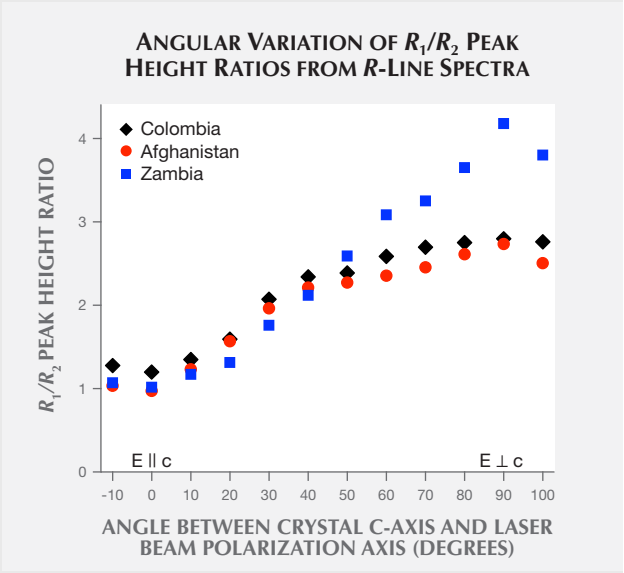

Figure A-4. The angular variation of R_1/R_2 *peak height ratios extracted from* R*-line spectra of emerald crystals from the three geographic origins.*

Finally, a plot of each sample's R_1/R_2 peak height ratio on an angular scale (figure A-4) shows that this ratio varies across the entire angular range from E ⊥ c orientation to E ∥ c orientation. For all three samples, the maximum value of this ratio occurs at the E ⊥ c orientation and the minimum value occurs at the E ∥ c orientation.

These comparisons of *R*-line spectral parameters at different angles explain why the present study concentrates on peak wavelengths extracted from E ⊥ c spectra. The primary reason is that the E ⊥ c orientation leads to the widest spread in R_1 peak positions. Nearly as important from a measurement perspective is that a slight misalignment away from this orientation will not alter the values of these peak wavelengths. Similarly, the R_2 peak position measurements at the E ⊥ c orientation are slightly more resistant to small misalignment.

In contrast to *R*-line peak wavelengths, values for the R_1/R_2 peak height ratios are sensitive to the angle between the crystal's c-axis and the excitation beam's polarization. While this sensitivity makes the R_1/R_2 peak height ratio a useful check of angular alignment, here we need not consider this peak parameter any further.

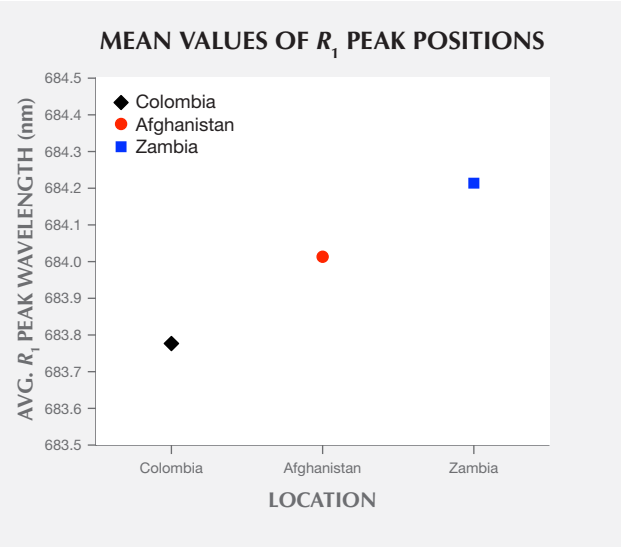

Figure 6. Mean values of R_1 *peak positions extracted from the* R*-line spectra of emerald samples from three regions. The black diamond corresponds to the mean value of 20 Colombian samples, the red circle to the mean value of 16 Afghan samples, and the blue square to the mean value of 12 Zambian samples. The error bars identify maximum and minimum wavelength values recorded for samples from each region.*

An independent sample *t* test was also performed between Afghan and Zambian samples. Similarly, there were extremely significant differences in the distributions for the Afghan (N = 16, M = 684.013 nm, SD = 0.084 nm) and Zambian samples (N = 12, M = 684.214 nm, SD = 0.046 nm); t(26) = 7.46, $p < 0.0001$, 95% CI [0.145 nm, 0.255 nm]. Once again, the low *p* value between this pair of sample datasets indicates that the measured difference between peak wavelengths probably does not arise from an accident of sampling.

Comparing the R_1 peak wavelengths dataset with each trace element concentration dataset (table 1) provided by GIA, the Mg and Na concentration datasets have very strong correlations with the R_1 peak wavelengths dataset. Each concentration dataset has the same coefficient of determination with the wavelengths dataset, namely $r^2 = 0.83$. By contrast, comparisons between the R_1 peak wavelengths dataset and all other trace element concentration datasets yield values for coefficients of determinations below 0.64.

A plot of all samples' R_1 peak wavelength vs. Mg concentration (figure 7) illustrates the first correlation. For this case, the best-fit trend line resulting from linear regression predicts a minimum R_1 peak wavelength (with no Mg concentration) of 683.65 nm and a peak shift of 0.048 nm per 1000 ppma increase in Mg concentration. The scatterplot also outlines the trend line's 95% confidence band, where a new data point collected from a random sample is predicted to fall within this band 19 times out of 20 (Natrella, 2013).

Very similar correlation is seen in a plot of all samples' R_1 peak wavelength vs. Na concentration (figure 8). The trend line here predicts nearly the same minimum R_1 peak wavelength (with no Na concentration) of 683.66 nm and a peak shift of 0.041 nm per 1000 ppma increase in Na concentration. The scatterplot also shows this trend line's 95% confidence band.

Returning to the *R*-line spectra (figure 5), the Colombian and Afghan samples' R_2 lines peak at similar wavelengths, while the Zambian sample's line is shifted to a shorter wavelength. A plot of the mean R_2 peak wavelength of samples from each origin (figure 9) shows that Colombian and Afghan samples' mean peak positions are overlapped by the extreme values in their distributions. In contrast, the mean peak position of Zambian samples is shifted to

Figure 7. A plot of each sample's R_1 *peak wavelength vs. Mg concentration. The coefficient of determination between these two datasets is* $r^2 = 0.83$. *The solid black trend line has a slope of 0.049 nm/1000 ppma and an intercept at 683.65 nm. The two dashed green lines outline the 95% confidence band for predictions using the best-fit trend line.*

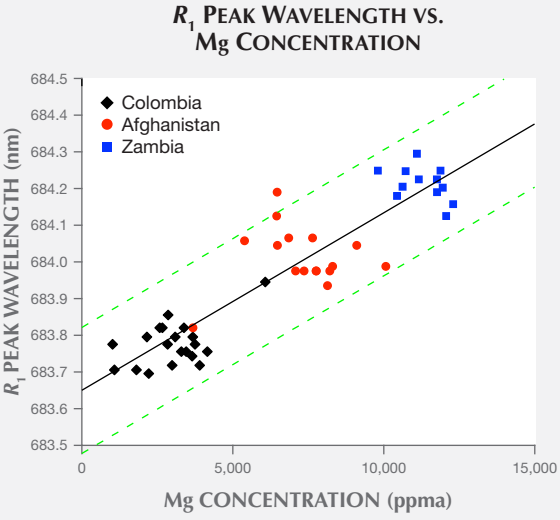

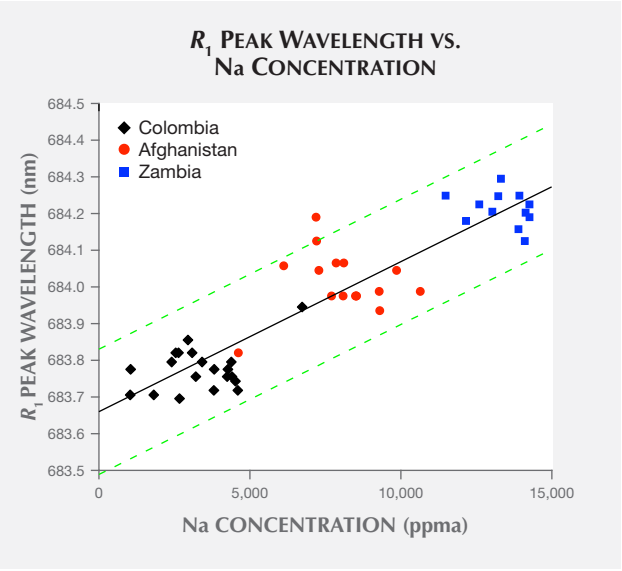

Figure 8. A plot of each sample's R_1 *peak wavelength vs. Na concentration. The coefficient of determination between these two datasets is* $r^2 = 0.83$. *The solid black trend line has a slope of 0.041 nm/1000 ppma and an intercept at 683.66 nm. The two dashed green lines outline the 95% confidence band for predictions using the best-fit trend line.*

a shorter wavelength and is not overlapped by the other samples' distributions.

To compare R_2 peak wavelength distributions between Afghan and Zambian samples, independent sample *t* tests were performed. The results show extremely significant differences in the distributions for the Afghan (N = 16, M = 680.699 nm, SD = 0.042 nm) and Zambian samples (N = 12, M = 680.461 nm, SD = 0.041 nm); t(26) = 15.00, $p < 0.0001$, 95% CI [0.205 nm, 0.270 nm]. Here, the *p* value for the Afghan and Zambian samples indicates little probability that they share the same mean value for R_2 peak wavelength.

An independent sample *t* test was also performed between Colombian and Afghan samples. The results show no significant differences in the distributions for the Colombian (N = 20, M = 680.712 nm, SD = 0.047 nm) and Afghan samples (N = 16, M = 680.699 nm, SD = 0.042 nm); t(34) = 0.87, $p = 0.39$, 95% CI [0.017 nm, 0.044 nm]. This high *p* value for the Colombian and Afghan samples indicates significant probability that they may share the same mean value for R_2 peak wavelength.

When the R_2 peak wavelengths dataset is compared with each trace element concentration dataset, Li ion concentration (table 1) has the strongest correlation, with coefficient of determination $r^2 = 0.79$. The Na ion concentration dataset also shows strong correlation with R_2 peak wavelengths, with coefficient of determination $r^2 = 0.68$. The coefficients of determination between the R_2 peak wavelengths dataset and all other trace element concentration datasets have values well below 0.64. A plot of R_2 peak wavelength vs. Li concentration (figure 10) illustrates their correlation. Here the best-fit trend line predicts a maximum R_2 peak wavelength (with no Li concentration) of 680.74 nm and a peak shift of –0.154 nm per 1000 ppma increase in Li concentration. The scatterplot also shows this trend line's 95% confidence band.

Examining the full set of PL emission spectra (again, see figure 3), it is apparent that even though the narrow *R* lines' structure varies from one location to another, the overall shape of the broadband structure is roughly similar. As the PL emission arises from Cr substituting at Al sites in the beryl crystal, we first consider if the peak count rate of this broadband structure (located at about 715 nm) might be directly proportional to the emerald sample's Cr concentration. A plot of all samples' broadband peak count rates vs. Cr concentration (figure 11) shows no evidence that they are directly propor-

Figure 9. Mean values of R_2 *peak positions extracted from the* R*-line spectra of emerald samples from the selected countries. The black diamond corresponds to the mean value of 20 Colombian samples, the red circle to 16 Afghan samples, and the blue square to 12 Zambian samples. The error bars identify maximum and minimum wavelength values recorded for each region.*

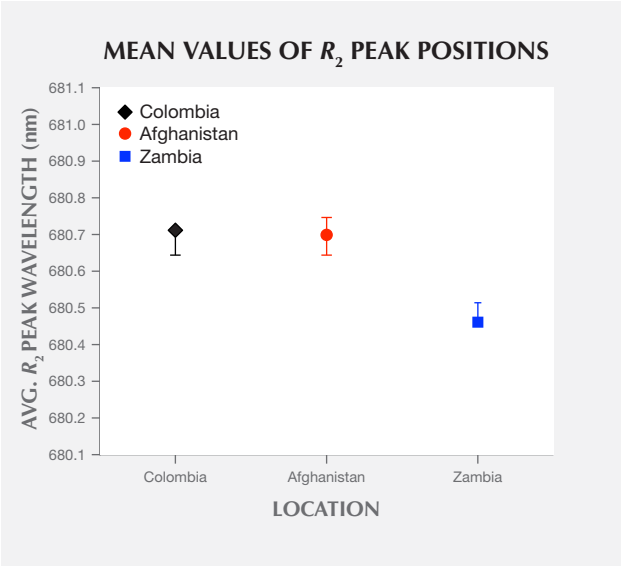

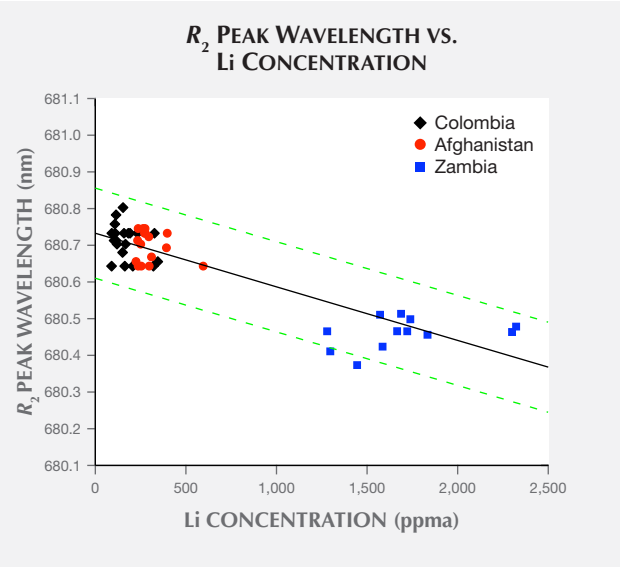

Figure 10. A plot of each sample's R_2 peak wavelength vs. Li concentration. The coefficient of determination between these two datasets is $r^2 = 0.79$. The solid black trend line has a slope of –0.154 nm/1000 ppma and an intercept at 680.74 nm. The two dashed green lines outline the 95% confidence band for predictions using the best-fit trend line.

tional. In this plot, most Colombian samples have low Cr concentrations and high count rates. Then there were Zambian samples that had high Cr concentrations and very low count rates, and Afghan samples appear all over the plot. Granted, the peak count rate does also depend upon the PL collection efficiency of the instrument. But with the luminescence collection volume (defined by the overlap of light beam, emerald, and optical fiber field of view) confined along one edge of the emerald, and with an effort to position the emerald edge to maximize these count rates, we do not expect much variation in collection efficiency.

As mentioned earlier, Fe ions can also substitute at Al cation sites in the beryl crystal, and it is well known that Fe dissipates PL emission by Cr (Nassau, 1978). A plot of all samples' broadband peak count rates vs. Fe concentration (figure 12) shows that count rates drop exponentially with increasing Fe concentration. Thus, the high Fe concentration in Zambian emeralds explains the low values of their observed count rates.

Following these examinations, we attempted to construct an empirical model where peak count rate was proportional to Cr concentration and decayed exponentially with increasing Fe concentration. In testing this model against our data, we found that peak count rate was better predicted when it was proportional to the square root of Cr concentration. The empirical formula we found that best predicts count rate I is

$$I = A\sqrt{[\mathrm{Cr}]} \cdot 10^{-\frac{[\mathrm{Fe}]}{B}} \qquad \text{(equation 1)}$$

where [Cr] and [Fe] are chromium and iron atomic concentrations, respectively (see box B). The empirical parameter B in the exponent is the Fe concentration that reduces Cr photoluminescence count rate by a factor of ten, while the parameter A represents the instrument's collection efficiency. Rewriting equation 1 as a linear function of iron concentration [Fe]

$$\log(I/\sqrt{[Cr]}) = -[Fe]/B + \log(A) \qquad \text{(equation 2)}$$

suggests plotting the common logarithm of each sample's $I/\sqrt{[Cr]}$ ratio vs. iron concentration (figure 13). This pair of datasets has a coefficient of determination $r^2 = 0.85$. Linear regression establishes values for the empirical parameters. The best-fit value for A is 1400, but this parameter is not much use beyond our experiment since it would have to be refitted for a different setup. The best-fit value for B is 2200 ppma Fe. This B parameter is independent of experimental setup, and it quantifies the low count rates observed

Figure 11. A plot of each sample's PL count rate at the 715 nm peak of broadband emission vs. chromium concentration. Colombian samples with low Cr concentrations exhibit high count rates, while Zambian samples with high Cr concentrations exhibit low count rates.

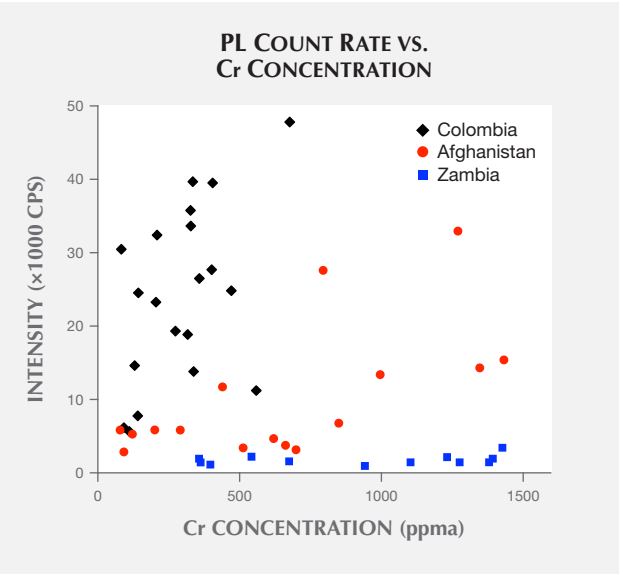

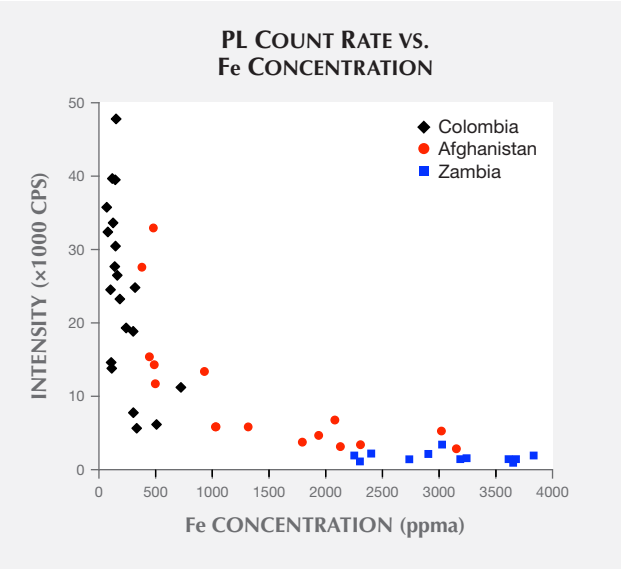

Figure 12. A plot of each sample's PL count rate at the 715 nm peak of broadband emission vs. iron concentration. Colombian samples with low Fe concentrations exhibit high count rates, while Zambian samples with high Fe concentrations exhibit low count rates. The general trend appears to be an exponential decay of count rate as Fe concentration increases.

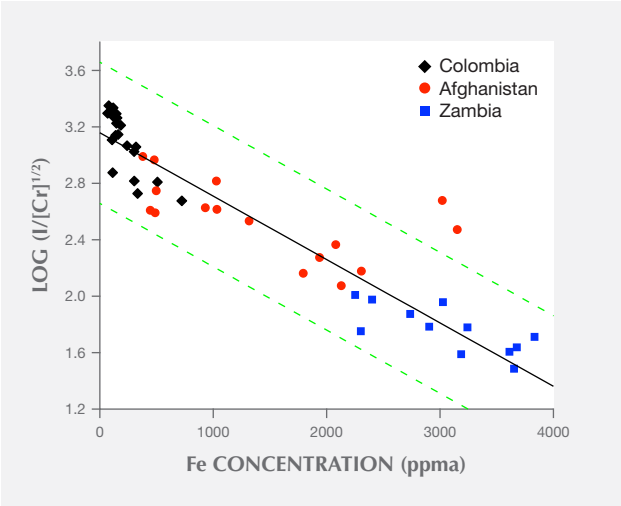

Figure 13. Dividing PL count rates of each sample's broadband peak emission I *by the square root of its chromium concentration [Cr], and taking the common logarithm, with the results plotted versus each sample's iron concentration [Fe]. These datasets have coefficient of determination* $r^2 = 0.85$. *Our model prediction suggests the data should follow a trend line given by equation 2 in the text, which contains empirical parameters* A *and* B. *The solid black trend line is a plot of equation 2 using the best-fit values for these parameters,* A = *1400 and* B = *2200 ppma Fe. The two dashed green lines outline the 95% confidence band for predictions using the best-fit trend line.*

from Zambian samples. In figure 13, all Zambian samples have Fe concentrations above the 2200 ppma concentration, reducing PL emission by a factor of ten; several samples have Fe concentrations above 3300 ppma concentration, reducing emission by a factor of 30. With the empirical parameters determined from regression, the empirical formula predicts count rates in our setup within a factor of two of all samples' observed count rates except for two Afghan samples. The formula underestimates count rates of these two samples by about a factor of six.

DISCUSSION

Using an *R*-line Wavelength Measurement to Reject a Possible Origin. *R*-line peak wavelength values extracted from the PL spectra of emeralds exhibit distributions that tend to be localized according to geographic origin. Here we consider how one might use these distributions as an aid to origin identification. Assuming each origin's measured distribution of *R*-line peak wavelengths represents that population's true normal probability distribution[2], we consider an *R*-line peak wavelength extracted from a random sample's PL spectrum. If the random sample's origin is completely unknown, and its origin might not be any of the three considered here, how can knowledge of the sample's *R*-line peak wavelength be used to reject one or more of these as possible origin assignments?

Answering this question requires setting a significance threshold. If a comparison of the sample's *R*-line measurement with an origin population's distribution has a *p* value that is less than the chosen significance threshold, then that population is rejected as a possible sample origin. Here the *p* value is the probability of measuring an *R*-line peak wavelength from a population's sample that is equal to or more extreme than what was actually measured (Kahn, 2016). Given the uncertainties in the mean values and standard deviations of distributions pre-

[2]One can use the number of measured samples (N) from the population to quantify how far the measured distribution may deviate from the population's true probability distribution by determining uncertainties in the measured distribution's mean and standard deviation (Natrella, 2013). The 95% CI uncertainties in mean values of R_1 peak wavelengths range from ±0.028 nm for Colombian samples to ±0.045 nm for Afghan samples; the same 95% CI uncertainties in standard deviations range from ±0.018 nm for Colombian samples to ±0.034 nm for Afghan samples.

Box B: Testing the Empirical Formula Relating PL Intensity to Cr and Fe Concentrations

To test the empirical formula represented by equations 1 and 2, we extracted broadband peak intensities from PL spectra collected from an additional nine natural emerald samples with different origins. These samples also were provided by GIA's Bangkok laboratory, and they were similarly altered with polished faces perpendicular to their c-axes. The laboratory also provided chemical concentrations of each sample, which were measured using LA-ICP-MS. Three of the samples were from the Chivor mine in Colombia, and another three from the Davdar emerald mines in China; these six samples were used in the report by Saeseaw et al. (2014). The last three samples were collected by GIA from the Swat Valley region of Pakistan but were not used in the Saeseaw report.

The results of this test appear in a scatterplot (figure B-1) showing the common logarithm of each test sample's $I/\sqrt{[Cr]}$ ratio vs. its Fe concentration. The test data shows general agreement with the corresponding trend line plot of equation 2 (using best-fit values of parameters listed in figure 13), with all data points located within the trend line's 95% confidence band. In addition, the empirical formula written as equation 1 predicts count rates for all test samples within a factor of two of their observed count rates.

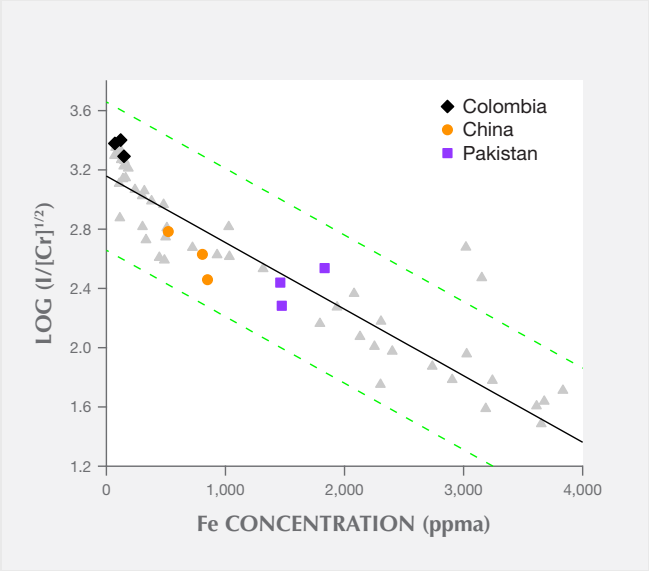

Figure B-1. Dividing PL count rates of each test sample's broadband peak emission I *by the square root of its chromium concentration* [Cr], *and taking the common logarithm, with the results plotted versus each test sample's iron concentration [Fe]. The black diamonds represent data from Colombian samples, the violet squares Pakistani samples, and the orange circles Chinese samples. The gray triangles reproduce the datasets presented in figure 13. The solid black trend line is a plot of the best-fit form of equation 2 to those datasets, and the dashed green lines form the boundaries of the equation's 95% confidence band.*

sented here, one might choose to set the significance threshold at an extreme value of 0.0001.

The rejection criterion can be simplified by using a *z* score. The *z* score between a measured value *x* and a population with mean M and standard deviation SD is given by $z = |x - M|/SD$, and it identifies how many standard deviations away from the mean the value *x* falls (Natrella, 2013). The range of probability values $p < 0.0001$ corresponds to a *z* score range of values $z > 3.70$ (Abramowitz and Stegun, 1972). If the *z* score between a random sample's *R*-line peak wavelength measurement and an origin population's peak wavelength distribution is greater than 3.70, then that population is rejected as a possible sample origin.

As an example, consider an extreme R_1 peak wavelength value that appeared in our Colombian dataset. The R_1 peak wavelengths of most Colombian samples cluster around the reported mean value M = 683.777 nm with standard deviation SD = 0.060 nm. But as shown in figures 7 and 8, one sample known to be of Colombian origin has an R_1 peak wavelength value *x* = 683.946 nm. Of the 20 Colombian samples reported here and six other examples reported by Thompson et al. (2014), this value is by far the most extreme recorded for a Colombian sample. The *z* score between this sample's R_1 peak wavelength and the Colombian distribution is $z = 2.817$, so it does not meet the threshold for rejection.

However, the z score between that sample's R_1 peak wavelength and the Afghan distribution is only $z = 0.798$, well below the rejection criterion. If the origin of this sample was truly unknown, we could not reject either Colombia or Afghanistan. In contrast, the z score between the sample's R_1 peak wavelength and the Zambian distribution is $z = 5.826$, which exceeds the threshold for rejection. Therefore, Zambia can be rejected as a possible origin.

As another example, could a sample with R_1 peak wavelength equal to $x = 684.000$ nm possibly be from Colombia? The z score between this R_1 peak wavelength and the Colombian distribution is $z = 3.717$, which exceeds the minimum z value for rejection. We therefore would reject Colombia as a possible origin for any sample with R_1 peak value at or above this wavelength.

Identifying a Mechanism Responsible for Shifts in R_1-Line Peak Wavelengths. We propose that the trace element dataset producing the highest coefficient of determination with a particular R-line dataset is most likely the impurity substitution responsible for shifting the R-line's peak wavelength. When two or more trace element datasets produce similar high values of r^2 with the R-line's dataset, we must consider how each may be involved with the R-line's peak shift.

As noted earlier, the shift in R_1 peak wavelength with increasing Mg and Na impurity concentrations shows very strong correlations, with the same coefficient of determination for both concentration datasets, $r^2 = 0.83$. These strong correlations suggest that the R_1 peak shift arises primarily from the aliovalent substitution of Mg at Al octahedral crystal sites, with charge balance provided by Na occupying an open channel site: $Al^{3+} \leftrightarrow Mg^{2+} + Na^{+}$.

Comparing the Mg and Na ion concentration datasets reveals that the presence of one ion correlates very strongly with the presence of the other, with a coefficient of determination $r^2 = 0.99$ between the two datasets. Yet a plot of Mg vs. Na concentration (figure 14) does not exhibit a one-to-one match, where each Mg ion would be accompanied by exactly one Na ion. In fact, the trend line resulting from linear regression reveals a slight excess of Na ions, where 10 Mg ions are matched by 11 Na ions. This 10% difference between Na and Mg ion concentrations may arise from a matrix effect in the LA-ICP-MS measurements (Sylvester, 2008). The efficiency with which different ions are ablated from the NIST glass matrix used for calibration may differ slightly from the efficiency of ions released by ablation from beryl matrix. If an excess of Na ions does not originate from a matrix effect, however, these ions may contribute to the R_2 peak shift, as described below.

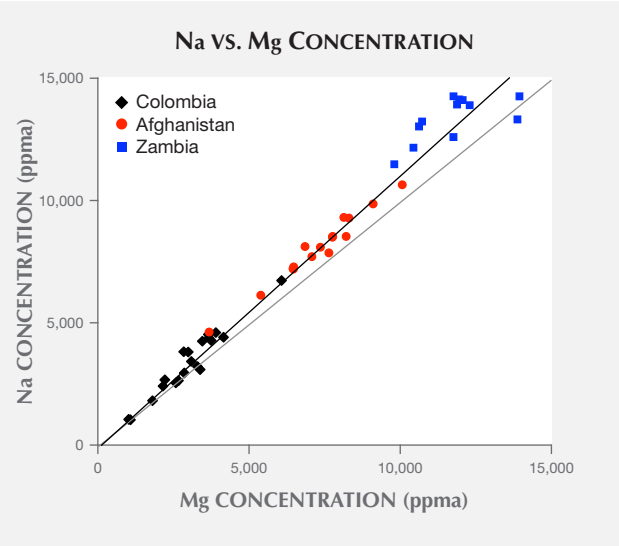

Figure 14. A plot of each sample's sodium vs. magnesium concentration. The coefficient of determination between these two datasets is $r^2 = 0.99$. *The black trend line has a slope of 1114 ppma Na/1000 ppma Mg. For comparison, the gray line has unit slope.*

Identifying a Mechanism Responsible for Shifts in R_2-Line Peak Wavelengths. As noted in the Results section, the R_2 peak wavelengths dataset exhibits strong correlation with the Li ion concentration dataset, with coefficient of determination $r^2 = 0.79$. The lack of correlation between R_2 peak positions and divalent and trivalent cation concentrations suggests that substitution at Al crystal sites is not responsible for the R_2 peak shift. Conversely, Li is the only cation that substitutes at the tetrahedral Be crystal site in beryl (Aurisicchio et al., 1988). To maintain charge balance, an accompanying alkali ion also must occupy an interstitial site. Besides Li concentrations, only the Na concentration dataset shows any significant correlation with the R_2 peak wavelengths dataset, with coefficient of determination $r^2 = 0.68$.

As described above, most Na atoms appear to be paired with Mg atoms. In attempting to isolate the "excess Na" concentration (comprised of those Na ions not paired with Mg) by subtracting Mg concentrations from corresponding Na concentrations, the resulting excess Na concentration dataset shows slightly stronger correlation with R_2 peak positions than does the full Na dataset, with coefficient of de-

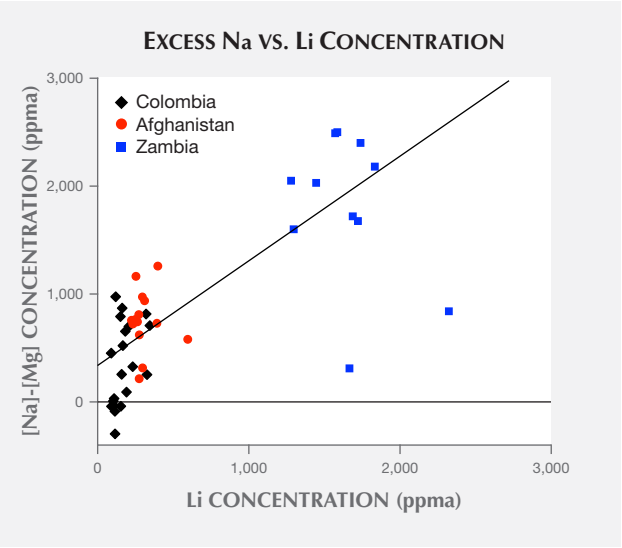

Figure 15. A plot of each sample's "excess Na" (the difference between sodium and magnesium concentrations) vs. lithium concentration. The coefficient of determination between these two datasets is r^2 = *0.66. The black trend line has a slope of 970 ppma Na/1000 ppma Mg and an intercept of 330 ppma excess Na.*

termination $r^2 = 0.72$. Adding the excess Na concentrations to corresponding Li concentrations creates even stronger correlation with R_2 peak positions, with coefficient of determination $r^2 = 0.83$. This coefficient of determination is higher than that achieved using the Li dataset by itself.

Comparing the Li and excess Na ion concentration datasets gives a coefficient of determination $r^2 = 0.66$, just barely exceeding the strong correlation threshold. A scatterplot of Li concentrations vs. excess Na concentration (figure 15), along with a best-fit trend line, demonstrates the correlation. The scatterplot does exhibit many outliers, including examples where subtracting a sample's Mg concentration from the corresponding Na concentration produces a slightly negative value. Overall, there appear to be several instances where there is not enough excess Na to match up with Li.

The strong correlation between samples' R_2 peak wavelengths and Li impurity concentrations suggests that the R_2 peak shift arises primarily from Li ions substituting at the tetragonal Be crystal sites. Interpreting correlations of excess Na impurity concentrations with the R_2 peak shift and with Li concentrations suggests that when Na ions are available, they may provide charge balance for the substitution. When Na ions are not available, we propose that the charge balance may be maintained by an additional Li ion occupying an open channel site: $Be^{2+} \leftrightarrow Li^+ + Na^+, Li^+$.

CONCLUSIONS

We have collected photoluminescence spectra of emerald samples from Colombia, Afghanistan, and Zambia. Extracting peak wavelengths of *R* lines appearing in emerald's E ⊥ c PL spectrum, we observed that values tend to be distributed according to geographic origin. With knowledge of localized distributions from a given origin, an *R*-line measurement of a random sample can provide evidence for or against the possibility of that origin.

Emerald samples from these three different origins were selected because they displayed distinctly different trace element impurity concentrations. Comparing peak positions of their *R* lines with corresponding concentrations of impurity ions, we have identified strong correlations between *R*-line peak shifts and increasing concentrations of specific impurities. In particular, the *R*-line peak wavelengths can also be used to estimate concentrations of three non-chromophore impurities in emerald: magnesium, sodium, and lithium. This assessment can supplement measurements of these impurities using other chemical composition analysis techniques, such as X-ray fluorescence, electron microprobe analysis, and LA-ICP-MS. The correlations also suggest likely mechanisms responsible for the *R*-line peak shifts.

Finally, comparing peak intensities of the broadband structure appearing in PL spectra with corresponding concentrations of chromium and iron impurities led to identification of an empirical formula where photoluminescence count rate increases with the square root of chromium concentration and decreases exponentially with increasing iron concentration. While it has long been known that iron impurities tend to quench chromium photoluminescence in gemstones, here we have quantified this effect.

ABOUT THE AUTHORS

Dr. Thompson is a professor in the department of physics and earth science at the University of North Alabama in Florence. Mr. Bayens worked with Dr. Thompson as an undergraduate researcher and is now a client systems engineer at Epic Systems in Madison, Wisconsin. Mr. Morgan, a former student of Dr. Thompson, is now an electronics engineer for the U.S. Army at Redstone Test Center in Huntsville, Alabama. Mr. Myrick is a student in electrical engineering at the University of Alabama in Tuscaloosa. Ms. Sims, a former student of Dr. Thompson, is a doctoral student in geophysics at the University of Alaska, Fairbanks.

ACKNOWLEDGMENTS

The authors thank Kenneth Scarratt for making emerald samples available for study. We also appreciate Vincent Pardieu for his support in providing samples. We are deeply grateful to Sudarat (Kai) Saeseaw for preparing samples and for providing their chemical concentration measurements. Lastly, we thank H. David Muse for checking the veracity of our statistical inferences.

REFERENCES

Abramowitz M., Stegun I.A. (1972) *Handbook of Mathematical Functions*. NBS Applied Mathematical Series 55, National Bureau of Standards, Washington, DC, Table 26.1, pp. 966–972.

Aurisicchio C., Fioravanti G., Grubessi O., Zanazzi P.F. (1988) Reappraisal of the crystal chemistry of beryl. *American Mineralogist*, Vol. 73, No. 7-8, pp. 826–837.

Crow E.L., Davis F.L., Maxfield M.W. (1960) *Statistics Manual*. Dover Publications, Mineola, New York.

Giuliani G., Ohnenstetter D., Fallick A.E., Groat L.A., Feneyrol J. (2012) Geographic origin of gems linked to their geological history. *InColor*, Vol. 19, pp. 16–27.

Goldman S.D., Rossman G.R., Parkin K.M. (1978) Channel constituents in beryl. *Physics and Chemistry of Minerals,* Vol. 3, No. 3, pp. 225–235, http://dx.doi.org/10.1007/BF00633572

Groat L.A., Giuliani G., Marshall D.D., Turner D. (2008) Emerald deposits and occurrences: A review. *Ore Geology Reviews*, Vol. 34, No. 1, pp. 87–112, http://dx.doi.org/10.1016/j.oregeorev.2007.09.003

Kahn D.S. (2016) *Attacking Probability and Statistics Problems*. Dover Publications, Mineola, New York, pp. 74–82.

Lai S.T. (1987) Highly efficient emerald laser. *Journal of the Optical Society of America B: Optical Physics*, Vol. 4, No. 8, pp. 1286–1290, http://dx.doi.org/10.1364/JOSAB.4.001286

Moroz I., Roth M., Boudeulle M., Panczer G. (2000) Raman microspectroscopy and fluorescence of emeralds from various deposits. *Journal of Raman Spectroscopy*, Vol. 31, No. 6, pp. 485–490, http://dx.doi.org/10.1002/1097-4555(200006)31:6%3C485::AID-JRS561%3E3.0.CO;2-M

Nassau K. (1978) The origins of color in minerals. *American Mineralogist*, Vol. 63, No. 3-4, pp. 219–229.

Natrella M.G. (2013) *Experimental Statistics*. Dover Publications, Mineola, New York.

O'Haver T.C. (2014) Peak finding and measurement [computer software]. *A Pragmatic Introduction to Signal Processing*. College Park, MD, http://terpconnect.umd.edu/~toh/spectrum/PeakFindingandMeasurement.htm

Saeseaw S., Pardieu V., Sangsawong S. (2014) Three-phase inclusions in emerald and their impact on origin determination. *G&G*, Vol. 50, No. 2, pp. 114–132, http://dx.doi.org/10.5741/GEMS.50.2.114

Schmetzer K. (1994) Torrington emerald update. *Australian Gemmologist*, Vol. 18, No. 10, pp. 318–319.

Schmetzer K. (2015) Letters: Photoluminescence of emeralds: Sample orientation procedure and correlation of the R1 peak position with SiO_2 contents. *Journal of Gemmology*, Vol. 34, No. 5, pp. 441–443.

Schmetzer K., Bernhardt H.-J. (1994) Isomorphic replacement of Al and Si in tetrahedral Be and Si sites of beryl from Torrington, NSW, Australia. *Neues Jahrbuch für Mineralogie Monatshefte*, Vol. 3, pp. 121–129.

Schwarz D., Schmetzer K. (2002) The definition of emerald–the green variety of beryl colored by chromium and/or vanadium. In Extralapis: Emeralds of the World, *extraLapis English* No. 2, Lapis International, East Hampton, Connecticut.

Sylvester P.J. (2008) Matrix effects in laser ablation-ICP-MS. In P.J. Sylvester, Ed., *Laser Ablation ICP-MS in the Earth Sciences: Current Practices and Outstanding Issues (Short Course)*. Vol. 40, Mineralogical Association of Canada, pp. 67–78.

Thomas T. (2009) Corundum c-axis device for sample preparation. *GIA Research News*, http://www.gia.edu/gia-news-research-nr6809

Thompson D.B., Kidd J.D., Åström M., Scarani A., Smith C.P. (2014) A comparison of R-line photoluminescence of emeralds from different origins. *Journal of Gemmology*, Vol. 34, No. 4, pp. 334–343.

Wood D.L. (1965) Absorption, fluorescence, and Zeeman effect in emerald. *Journal of Chemical Physics*, Vol. 42, No. 10, pp. 3404–3410, http://dx.doi.org/10.1063/1.1695742